PNAS RESEARCH ARTICLE | CHEMISTRY MEDICAL SCIENCES

Toward quantification of hypoxia using fluorinated $Eu^{II/III}$-containing ratiometric probes

S. A. Amali S. Subasinghe[a], Caitlyn J. Ortiz[b], Jonathan Romero[b], Cassandra L. Ward[c], Alexander G. Sertage[a], Lyazat Kurenbekova[d], Jason T. Yustein[e,1], Robia G. Pautler[b,1], and Matthew J. Allen[a,1]

Edited by Kenneth Raymond, University of California, Berkeley, CA; received December 8, 2022; accepted March 7, 2023

Hypoxia is a prognostic biomarker of rapidly growing cancers, where the extent of hypoxia is an indication of tumor progression and prognosis; therefore, hypoxia is also used for staging while performing chemo- and radiotherapeutics for cancer. Contrast-enhanced MRI using Eu^{II}-based contrast agents is a noninvasive method that can be used to map hypoxic tumors, but quantification of hypoxia using these agents is challenging due to the dependence of signal on the concentration of both oxygen and Eu^{II}. Here, we report a ratiometric method to eliminate concentration dependence of contrast enhancement of hypoxia using fluorinated $Eu^{II/III}$-containing probes. We studied three different $Eu^{II/III}$ couples of complexes containing 4, 12, or 24 fluorine atoms to balance fluorine signal-to-noise ratio with aqueous solubility. The ratio between the longitudinal relaxation time (T_1) and ^{19}F signal of solutions containing different ratios of Eu^{II}- and Eu^{III}-containing complexes was plotted against the percentage of Eu^{II}-containing complexes in solution. We denote the slope of the resulting curves as hypoxia indices because they can be used to quantify signal enhancement from Eu, that is related to oxygen concentration, without knowledge of the absolute concentration of Eu. This mapping of hypoxia was demonstrated in vivo in an orthotopic syngeneic tumor model. Our studies significantly contribute toward improving the ability to radiographically map and quantify hypoxia in real time, which is critical to the study of cancer and a wide range of diseases.

hypoxia | MRI | ratiometric | responsive contrast agents

Significance

This study reports dual-mode probes that enable ratiometric quantification of hypoxia in a concentration-independent manner based on the magnetic and electronic differences between Eu^{II} and Eu^{III}. These results are significant because hypoxia is an important biomarker in a wide range of diseases and there is a critical need to spatially quantify hypoxia to improve our biological understanding of these diseases and identify and evaluate new treatments.

Tumor hypoxia develops because of uncontrollable cell proliferation and abnormal vasculature that fails to transport oxygen to the interior cells of tumors (1–3). To dwell in reduced oxygen concentrations, hypoxic cells adjust their cellular environment to possess different chemical and physiological characteristics compared to normoxic cells (4–6). These adaptations lead to poor prognosis, tumor aggressiveness, and therapeutic resistance (7), making hypoxia an important biomarker in the diagnosis of cancer (8). Several imaging modalities have been used to image hypoxia including positron emission tomography, X-ray computed tomography, single-photon emission tomography, optical imaging, and MRI (9–13). The use of MRI is advantageous because it uses nonionizing radiowaves to generate three-dimensional images with near-cellular spatial resolution. Contrast agents are often used in MRI to overcome its inherent poor sensitivity, and responsive contrast agents can be designed to provide molecular information by changing the degree or type of contrast enhancement in response to a molecular event or the presence or absence of an analyte, like O_2 (14–20). One of the most promising types of contrast agents for imaging O_2 involves Eu^{II} (21–26). This ion enhances contrast-like clinically used Gd^{III}, but unlike Gd^{III}, Eu^{II} oxidizes to Eu^{III}, an ion that does not enhance contrast in T_1-weighted MRI. Thus, the ion provides a clear switch with respect to responsive imaging of O_2.

However, the use of contrast-enhanced MRI with responsive contrast agents in tumor imaging is limited because of the dependence of contrast enhancement on the concentration of contrast agents, which is extremely difficult to measure in vivo. Because of this limitation, differentiation between complete response, partial response, and no response is muddled during in vivo MRI (27, 28). Therefore, there is a critical need to employ new strategies to overcome concentration-related limitations to enable responsive contrast-enhanced MRI of hypoxia. In general, several strategies have been used to address concentration dependency of contrast-enhanced MRI (29–33). One of the most promising strategies is the use of ratiometric methods (34–38). Signals arising from individual probes depend on the concentration of a contrast agent; however, the ratio between the concentration-dependent responses causes concentration to become irrelevant if the contrast agent is present above the minimum detectable threshold. Consequently, we hypothesized that dual-mode responsive contrast agents based on ^1H- and ^{19}F-MRI coupled with europium in the +2 and +3 oxidation states would enable ratiometric imaging of hypoxia.

Author contributions: S.A.A.S.S., J.T.Y., R.G.P., and M.J.A. designed research; S.A.A.S.S., C.J.O., J.R., C.L.W., A.G.S., L.K., and R.G.P. performed research; S.A.A.S.S., J.T.Y., R.G.P., and M.J.A. analyzed data; and S.A.A.S.S., C.J.O., J.R., C.L.W., A.G.S., L.K., J.T.Y., R.G.P., and M.J.A. wrote the paper.

The authors declare no competing interest.

This article is a PNAS Direct Submission.

[1]To whom correspondence may be addressed. Email: jason.yustein@emory.edu, rpautler@bcm.edu, or mallen@chem.wayne.edu.

This article contains supporting information online at https://www.pnas.org/lookup/suppl/doi:10.1073/pnas.2220891120/-/DCSupplemental.

Published April 5, 2023.

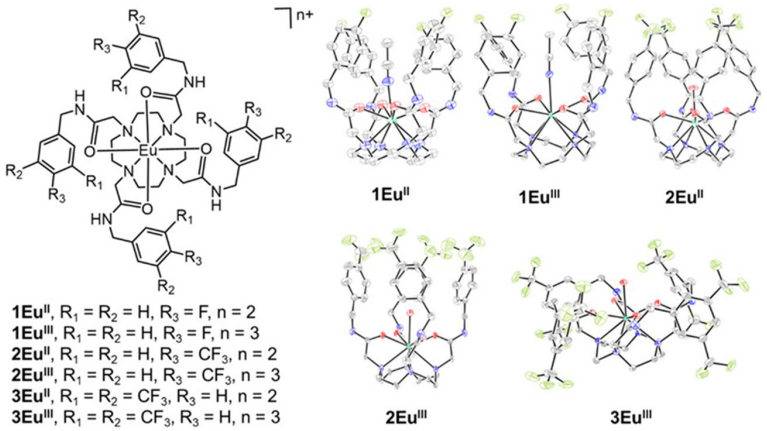

Fig. 1. (*Left*) Chemical structures of **1Eu**^{II},**1Eu**^{III}, **2Eu**^{II}, **2Eu**^{III}, **3Eu**^{II}, and **3Eu**^{III}. (*Right*) Molecular structures in crystals of **1Eu**^{II}, **1Eu**^{III}, **2Eu**^{II}, **2Eu**^{III}, and **3Eu**^{III}. Chloride counterions, outer-sphere water molecules, and hydrogen atoms are not shown for clarity. Thermal ellipsoids are drawn at 50% probability. Gray = C; blue = N; red = O; yellow-green = F; sea green = Eu. Crystallographic data for these structures have been deposited at the Cambridge Crystallographic Data Centre under deposition numbers 2203173 (**1Eu**^{II}), 2203172 (**1Eu**^{III}), 1562330 (**2Eu**^{II}), (22) 1562331 (**2Eu**^{III}), (22) and 2203174 (**3Eu**^{III}).

Here, we report the testing of this hypothesis using fluorinated Eu^{II}- and Eu^{III}-containing complexes with varying local concentrations of fluorine (Fig. 1).

Results and Discussion

Inspired by reported fluorinated europium-containing complexes (22, 39), we synthesized ligands **1**–**3** that vary in the number of chemically equivalent fluorine atoms. Chemical equivalency of fluorine atoms is important to avoid diluting signal during imaging. Additionally, the presence of more chemically equivalent fluorine atoms is associated with increased sensitivity in imaging; however, the presence of more fluorine atoms is also associated with decreased aqueous solubility. Consequently, ligands **1**–**3** were selected to provide a range of fluorine atoms to balance these two important parameters. The tetra-amide binding site of the ligand was selected because it forms inert complexes with both Eu^{II} and Eu^{III} (23).

Fluorinated ligands were synthesized in two steps from commercially available starting materials. Ligands **1** and **2** were synthesized using reported procedures (22, 39), and ligand **3** was synthesized and characterized using ^{1}H-, ^{13}C-, and ^{19}F-NMR spectroscopy and high-resolution mass spectrometry (see *SI Appendix* for details). Ligands were metalated with $EuCl_3{\cdot}6H_2O$ to produce **1Eu**^{III}, **2Eu**^{III}, and **3Eu**^{III}. The reduced versions of those complexes — **1Eu**^{II}, **2Eu**^{II}, and **3Eu**^{II}— were prepared in quantitative yield by reducing the corresponding Eu^{III}-containing complexes with Zn^0 (see the electronic supplementary information for detailed procedures, yields, and characterization).

To study the structures of the six complexes, X-ray crystallography was performed on single crystals of the complexes. In the structures, all the four amide arms of **1Eu**^{II}, **1Eu**^{III}, **2Eu**^{II}, and **2Eu**^{III} are pseudoaxial, resulting in caged structures around monodentate ligands coordinated to the Eu ions. This cage formation can be attributed to the fluorophilic character of the F and CF_3 groups and π-stacking of the benzene rings. The amide arms of **3Eu**^{II} and **3Eu**^{III} are pseudoequatorial due to steric hindrance from the multiple CF_3 groups on each arm. These structures are expected given the reports of other tetraamide complexes of lanthanides (40–42). Importantly, the crystal structures confirmed the oxidation state of Eu, and each complex has a coordinated solvent molecule, water or acetonitrile, suggesting that they would be appropriate for contrast enhancement in ^{1}H-MRI.

To test the hypoxia-responsive nature of the complexes, we prepared solutions (1 mM) of Eu^{II}- and Eu^{III}-containing complexes of **1**, **2**, and **3** in aqueous 3-morpholinopropane-1-sulfonic acid buffer, pH 7.4, and mixed them to obtain solutions that were 0, 25, 50, and 75% $Eu^{II}_{(aq)}$ with respect to the total concentration of Eu in any oxidation state. We measured the T_1 relaxation times (influenced by Eu^{II} but not Eu^{III}) and the ^{19}F signals (influenced by Eu^{III} but not Eu^{II}) of the solutions. The ^{19}F signals were compared to those of an external standard of trifluoroacetic acid to calculate the number of ^{19}F nuclei.

Using the measured T_1 times and ^{19}F signals for the series of mixtures of oxidation states, we were able to derive a ratiometric ratio. The observed relaxation rate of the solution ($1/T_{1,obs}$) is related to the paramagnetic ($1/T_{1,p}$) and diamagnetic ($1/T_{1,d}$) relaxation rates (Eq. **1**), and rearrangement of Eq. **1** yields Eq. **2**. The diamagnetic relaxation rate is a property of the solvent, but in dilute Eu^{II}-containing solutions, the paramagnetic term $1/T_{1,p}$ is proportional to the concentration of Eu^{II} (Eq. **3**). Combining Eqs. **2** and **3** yields Eq. **4**.

$$\frac{1}{T_{1,obs}} = \frac{1}{T_{1,d}} + \frac{1}{T_{1,p}}, \quad [1]$$

$$1/T_{1,p} = 1/T_{1,obs} - 1/T_{1,d}, \quad [2]$$

$$\frac{1}{T_{1,p}} \propto \left[Eu^{II}\right], \quad [3]$$

$$1/T_{1,obs} - 1/T_{1,d} \propto \left[Eu^{II}\right]. \quad [4]$$

Fluorine signal is generated due to the presence of the Eu^{III}-containing complex in solution, and this signal is proportional to the number of moles of ^{19}F nuclei ($n^{19}F$) in the sample, and hence, to the concentration of the Eu^{III}-containing complex (Eq. **5**).

$$n^{19}F \propto \left[Eu^{III}\right]. \quad [5]$$

The sum of the percentage of Eu^{II} and Eu^{III} is 1 because those are the only two sources of Eu (Eq. **6**). Rearrangement of Eq. **6** results in Eq. **7**, which when combined with Eq. **5** yields Eq. **8**.

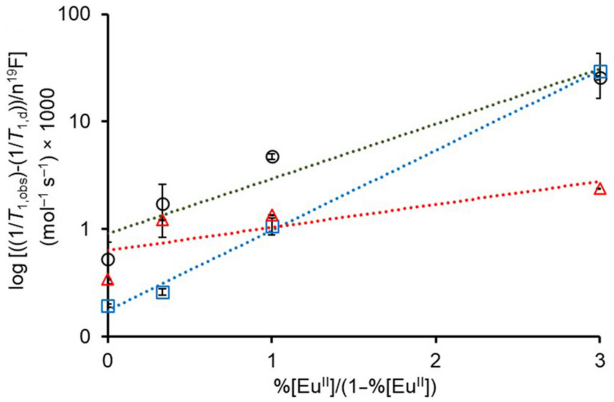

Fig. 2. Plots used to determine hypoxia indices (slopes) using T_1 and ^{19}F MR data from mixtures of **XEu**^{II} and **XEu**^{III} [**X** = **1** (blue, □), **2** (black, ○), and **3** (red, Δ) in aqueous 3-morpholinopropane-1-sulfonic acid buffer (pH 7.4)].

$$\%\left[Eu^{II}\right] + \%\left[Eu^{III}\right] = 1, \quad [6]$$

$$\%\left[Eu^{III}\right] = 1 - \%\left[Eu^{II}\right], \quad [7]$$

$$n^{19}F \propto 1 - \%\left[Eu^{II}\right]. \quad [8]$$

Both $1/T_{1,p}$ and ^{19}F measurements are dependent on the concentration of the probes; however, by taking the ratio of the two measurements (Eq. **3** divided by Eq. **8**), the concentration of the complex becomes inconsequential (Eq. **9**). We defined the proportionality constant, H_I, as the *hypoxia index* (units of mol^{-1} s^{-1}) to equate the two sides of the proportionality in Eq. **9** to yield Eq. **10**. Combination of Eq. **2** with Eq. **10** yields Eq. **11** in which $T_{1,obs}$, $T_{1,d}$, and ^{19}F signals are obtained using an MRI scanner.

$$\frac{\frac{1}{T_{1,p}}}{n^{19}F} \propto \frac{\left[Eu^{II}\right]}{1 - \%\left[Eu^{II}\right]}, \quad [9]$$

$$\frac{\frac{1}{T_{1,p}}}{n^{19}F} = H_I\left(\frac{\left[Eu^{II}\right]}{1 - \%\left[Eu^{II}\right]}\right), \quad [10]$$

$$\frac{1/T_{1,obs} - 1/T_{1,d}}{n^{19}F} = H_I\left(\frac{\left[Eu^{II}\right]}{1 - \%\left[Eu^{II}\right]}\right). \quad [11]$$

To test Eq. **11** with our data, we plotted the logarithm of $\frac{1/T_{1,obs} - 1/T_{1,d}}{n^{19}F}$ versus $\frac{\left[Eu^{II}\right]}{1-\%\left[Eu^{II}\right]}$ for each system that contains mixtures of **1Eu**^{II}, **1Eu**^{III}, **2Eu**^{II}, **2Eu**^{III}, **3Eu**^{II}, and **3Eu**^{III}(Fig. 2). All the three plots can be fit with straight lines with hypoxia indices (slopes) of 0.59 ± 0.06, 0.43 ± 0.06, and 0.17 ± 0.06 mol^{-1} s^{-1} for the systems containing **1Eu**^{II}/**1Eu**^{III}, **2Eu**^{II}/**2Eu**^{III}, and **3Eu**^{II}/**3Eu**^{III}, respectively. Based on the hypoxia indices, **1Eu**^{II}/**1Eu**^{III} possesses the steepest slope with **2Eu**^{II}/**2Eu**^{III} and **3Eu**^{II}/**3Eu**^{III} having slopes that are 27 and 71%, respectively, less steep. This result can be explained by the denominator of the left side of Eq. **11**, which is the number of moles of ^{19}F atoms in each system. A plot of the number of ^{19}F atoms (4, 12, or 24) per molecule versus the hypoxia indices (0.59, 0.43, and 0.17 mol^{-1} s^{-1}) yields a linear correlation, demonstrating that the number of ^{19}F atoms is the major driver of the slope. This dominance of ^{19}F is not surprising given the similar relaxivities of **1Eu**^{II}, **2Eu**^{II}, and **3Eu**^{II}. Steeper slopes are desirable because they enable more sensitive differentiation between regions with different concentrations of oxygen. Although our systems are concentration independent with respect to the amount of Eu, that only holds true for samples that are detectable. Further, the equation is limited to cases where some Eu^{II} is oxidized to Eu^{III} to avoid needing a zero in the denominator; in cases where Eu^{II} is not measurably oxidized, as determined by the presence of ^{19}F signal, then the area is extremely hypoxic. Despite **1Eu**^{II}/**1Eu**^{III} being the most sensitive with respect to slope of Eq. **11**, with only four fluorine atoms, the complex is difficult to detect at low millimolar concentrations. Consequently, for the rest of the studies in this report, we used **2Eu**^{II}/**2Eu**^{III} which has much better aqueous solubility than that of **3Eu**^{II}/**3Eu**^{III}. The known hypoxia indices, $T_{1,obs}$, $T_{1,d}$, and ^{19}F readouts from the scanner, can be used to determine %Eu^{II} in a given system as a measure of hypoxia.

To validate the concentration-independent nature of the hypoxia indices, the experiment was repeated at a concentration of 6 mM of Eu instead of 1 mM using the **2Eu**^{II}/**2Eu**^{III}system. The slope acquired at 6 mM was 0.49 ± 0.09 mol^{-1} s^{-1} (Fig. 3), which is not different from the slope measured at 1 mM (Student's *t* test results are included in the supporting information). These data demonstrate that the hypoxia index is a useful tool for measuring hypoxia in the absence of information about the concentration of Eu.

Inspired by our in vitro results, we wanted to learn the potential for application of our method in vivo. We chose **2Eu**^{II} for in vivo experiments because it has the best combination of ^{19}F signal, hypoxia index slope, and solubility among **1Eu**^{II}, **2Eu**^{II}, and **3Eu**^{II}. We performed intratumoral injections of **2Eu**^{II} (~150 μL, 6 mM in 3-morpholinopropane-1-sulfonic acid buffer, pH 7.4) to osteosarcoma in immunocompetent wild-type C57BL/6 mice using convection-enhanced delivery. Osteosarcoma was chosen because as a highly aggressive solid tumor, it develops areas of hypoxia secondary to outgrowing its blood supply. Further, there are strong links between hypoxia and chemotherapeutic resistance, promoting metastatic potential and alterations in immune microenvironment for osteosarcoma (43, 44). These hypoxia-mediated features are key facets that drive poor outcomes for patients and, thus, the immunocompetent osteosarcoma model provides an extremely valuable system to image and understand the role of hypoxia in tumor development progression (45). We measured $T_{1,obs}$ and ^{19}F signals. T_1-weighted MRI (Fig. 4) of the tumor showed the hypoxic region of the tumor. ^{19}F chemical shift imaging (CSI) map (Fig. 4) showed the normoxic region of the tumor, where **2Eu**^{II} is oxidized into **2Eu**^{III}. Overlaying of the T_1-weighted image with the ^{19}F CSI provided a complete picture of the tumor (Fig. 4). As a control for normoxic tissue, **2Eu**^{II} (100 μL, 6 mM) was injected into the thigh muscle of a healthy mouse, and ^{19}F signal was observed as expected (Fig. 4). Compared to limitations of biopsy, including invasiveness and ambiguous diagnosis of tumors, the method described here provides a platform for the quantification of relative levels of hypoxia in tumor microenvironments.

In conclusion, we report a method that enables quantify relative levels of hypoxia in tumor-bearing mice using fluorinated Eu-containing complexes without knowledge of the concentration of the contrast agent. We present hypoxia index curves for systems containing **1Eu**^{II}/**1Eu**^{III}, **2Eu**^{II}/**2Eu**^{III}, and **3Eu**^{II}/**3Eu**^{III} that serve

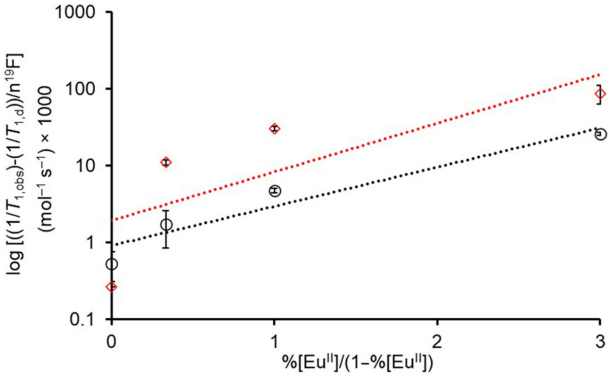

Fig. 3. Validation of the concentration-independent nature of the hypoxia indices using 1 and 6 mM solutions of **2Eu**^{II}/**2Eu**^{III} system. Based on a *t* test, there is no significant difference between hypoxia indices of 1 mM (black, ○) solution (0.43 mol^{-1} s^{-1}, R^2 = 0.9917) and 6 mM (red, ◊) solution (0.49 mol^{-1} s^{-1}, R^2 = 0.9183). The solutions were prepared in aqueous 3-morpholinopropane-1-sulfonic acid buffer (pH 7.4).

as calibration plots to quantify hypoxia in vivo. Our in vivo studies demonstrated that combined T_1-weighted MRI signal and ^{19}F signal can be used to characterize the extent of hypoxia in tumors by overcoming the concentration dependence of contrast agent. Coupled with studies involving the partial pressure of oxygen, which we are pursuing, we expect that these studies will provide the foundation for measuring hypoxia in a wide range of disease models that involve hypoxia, including studies involving tumor growth over time and models of ischemia. Further, the combination of these results with strategies that enable systemic delivery (21) would provide a path beyond studies requiring intratumoral injections.

Materials and Methods

Commercially available chemicals were of reagent-grade purity or better and were used without further purification unless otherwise noted. DOWEX-Na$^+$ was prepared as previously reported (23). Water was purified using a PURELAB Ultra Mk2 water purification system. Samples containing europium were prepared in a wet (water allowed but no O_2) glovebox under an atmosphere of N_2.

^{1}H-, ^{13}C-, and ^{19}F-NMR spectra were acquired using an Agilent A-400 (399.72 MHz for ^{1}H, 100.49 MHz for ^{13}C, and 376 MHz for ^{19}F) spectrometer or a Bruker BioSpec 9.4 T horizontal bore MRI scanner. Chemical shifts are reported relative to residual solvent signals or internal standard [CH_3OD: ^{1}H δ 3.31, ^{13}C δ 49.01, ^{19}F δ –78.20 (NaOTf internal standard in CH_3OD); $CDCl_3$: ^{1}H δ 7.27, ^{13}C δ 77.23, ^{19}F δ 0.00 ($CFCl_3$ internal standard in $CDCl_3$); D_2O: ^{1}H δ 4.79, ^{19}F: δ –78.20 (NaOTf internal standard in D_2O)]. NMR data are assumed to be first order and the multiplicity is reported as "s" = singlet, "d" = doublet, "q" = quartet, and "brs" = broad singlet. Italicized elements are those that are responsible for the shifts. Correlation spectroscopy, distortionless enhancement by polarization transfer, and heteronuclear multiple quantum coherence spectra were used to assign the spectral peaks.

Elemental analyses (C, H, and N) were performed by Midwest Microlab (Indianapolis). Thermal gravimetric analysis (TGA) was performed at 10 °C/min under flowing nitrogen using an SDT-2960 TGA and differential thermal analysis analyzer. Concentrations of Eu were determined using energy-dispersive X-ray fluorescence (EDXF) spectroscopy at the Lumigen Instrument Center

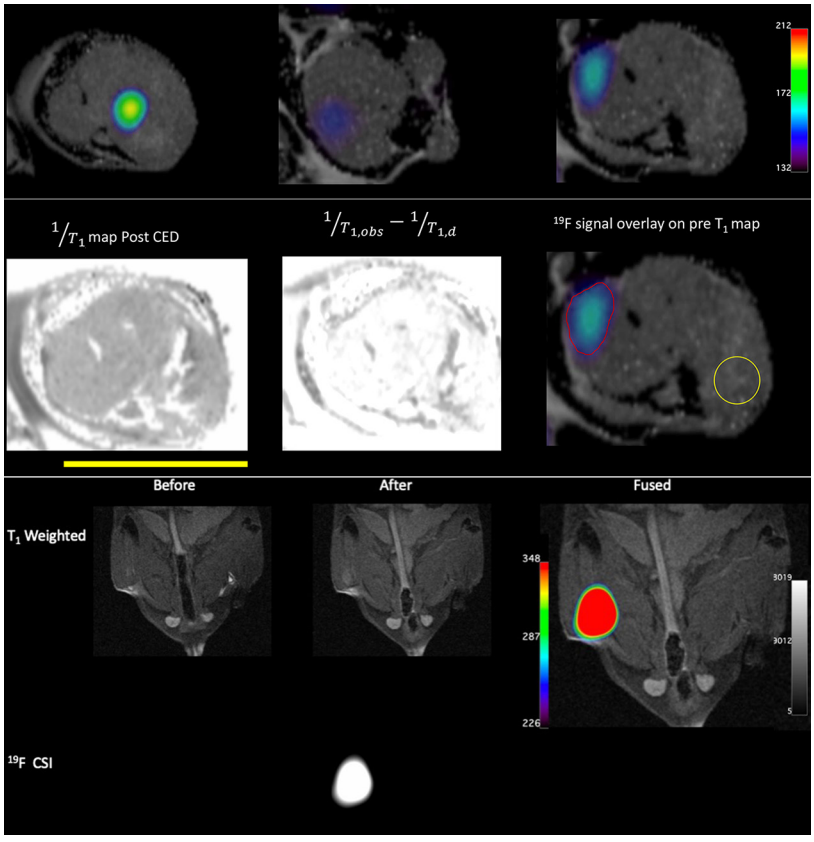

Fig. 4. In vivo imaging experiments of **2Eu**^{II}. (*Top* Row) Overlay of T_1-weighted ^{1}H-MRI and ^{19}F-MR images of osteosarcoma after convection-enhanced delivery of **2Eu**^{II}. The three images are from three slices across the tumor and show pockets of ^{19}F signal at different locations across the tumor. (*Middle* Row) Images of the rightmost slice from the *Top* row. The leftmost image is a $1/T_1$ map after convection-enhanced delivery of **2Eu**^{II}. The middle image is a difference map of $T_{1,obs}^{-1} - T_{1,d}^{-1}$ used to calculate the percent of Eu^{II} from Eq. **11**. The rightmost image is the overlay from the top image with two areas of interest denoted by red and yellow boundaries. ^{19}F atoms are observable inside the red boundary, and there is no detectable ^{19}F in the yellow circle. The combination of ^{19}F content with a hypoxia index of 0.43 mol^{-1} s^{-1} corresponds essentially to all Eu in the +2 oxidation state in the yellow circle and all Eu in the +3 oxidation state in the red circle. (*Bottom*) T_1-weighted MRI and ^{19}F CSI of thigh muscle of a healthy mouse injected with **2Eu**^{II} as a control for normoxic tissue. The yellow bar is 1 cm.

in the Department of Chemistry at Wayne State University. All dilutions were performed with 2% HNO_3, which was also used for blank samples during calibration. Calibration curves were created using the ^{153}Eu isotope ion count for 1 to 200 ppb concentration range (diluted from Fluka ICP standard solution). High-resolution electrospray ionization mass spectrometry (HRMS) was recorded using a waters LCT Premier Xe time-of-flight high-resolution mass spectrometer.

UV–visible absorbance spectra were measured using a Shimadzu UVmini-1240 spectrophotometer, and samples were loaded in quartz cuvettes under an atmosphere of N_2. Emission and excitation spectra were recorded using a HORIBA Jobin Yvon Fluoromax-4 spectrofluorometer. MRI studies were performed at Baylor College of Medicine. T_1-weighted and ^{19}F scans were performed with a Bruker BioSpec 9.4 T horizontal bore MRI scanner equipped with 20 cm bore. Images were acquired with a body coil while using a heater set to 37 °C.

Synthetic Procedures and Characterization. Eu^{II}- and Eu^{III}-containing complexes of 2,2,2,2-(1,4,7,10-tetraazacyclododecane-1,4,7,10-tetrayl)tetrakis(*N*-(4-(trifluoromethyl)benzyl)acetamide) (**2Eu**^{II} and **2Eu**^{III}, respectively) and Eu^{III}-containing complex of 2,2,2,2-(1,4,7,10-tetraazacyclododecane-1,4,7,10-tetrayl) tetrakis(*N*-(4-fluorobenzyl)acetamide) (**1Eu**^{III}) were synthesized following reported procedures (22, 39). Fluorinated tetraamide ligands and their corresponding Eu^{II}- and Eu^{III}-containing complexes were synthesized as shown in *SI Appendix*, Fig. S1. Characterization is reported in this manuscript for ligands and metal complexes that has not been reported elsewhere.

2-chloro-N-(3,5-bis(trifluoromethyl)benzyl)acetamide (6). To a stirring solution of (3,5-bis(trifluoromethyl)phenyl)methanamine (5.2500 g, 21.592 mmol) and K_2CO_3 (3.133 g, 22.672 mmol) in CH_2Cl_2 (100 mL) at 0 °C, a solution of chloroacetyl chloride (2.60 mL, 23.32 mmol) in CH_2Cl_2 (20 mL) was added dropwise. The resultant reaction mixture was stirred for 30 min at 0 °C followed by 30 min at ambient temperature. The mixture was filtered through a fine glass frit, and the solid was washed with CH_2Cl_2 (5 × 5 mL). The organic layer was washed with HCl (2 M, aqueous, 2 × 10 mL) followed by brine (3 × 10 mL), and the organic layer was dried over sodium sulfate. The solvent was removed under reduced pressure to yield a tan solid that was crystallized from CH_2Cl_2 to yield a white solid (2.967 g, 43%). ^1H NMR (399.72 MHz, $CDCl_3$): δ = 4.13 (s, 2H; ClCH_2), 4.62 (d, *J* = 4.0 Hz, 2H; NCH_2), 7.17 (brs, 1H; N*H*), 7.75 (s, 2H; C*H*), 7.81 (s, 1H; C*H*) ppm; ^{13}C NMR (100.49 MHz, $CDCl_3$): δ = 42.7 (ClCH_2), 43.1 (NCH_2), 121.9 (*C*H), 123.3 (q, ^1J = 272 Hz, *C*F_3), 127.8 (*C*H), 132.3 (q, ^2J = 33 Hz, *C*CF_3), 140.1, 166.7 ppm; ^{19}F NMR (376 MHz, $CDCl_3$): δ = –63.4 (s, CF_3) ppm; HRMS (*m*/*z*): $[M + H]^+$ calcd for $C_{11}H_8ClF_6NO$, 320.0277; found, 320.0274.

2,2′,2″,2‴-(1,4,7,10-tetraazacyclododecane-1,4,7,10-tetrayl)tetrakis (N-(4-(trifluoromethyl)benzyl)acetamide) (3). A stirring mixture of **6** (1.0000 g, 3.1286 mmol), K_2CO_3 (3.4539 g, 25.0288 mmol), cyclen (0.2520 g, 1.463 mmol), potassium iodide (0.010 mg, 0.060 mmol), and acetonitrile (150 mL) was heated to 120 °C. After 10 h, the mixture was filtered while hot through a fine glass frit, and the filtrate was concentrated under reduced pressure to yield a pale-yellow solid that was crystallized from acetonitrile to yield a white solid (2.082 g, 51%). ^1H NMR (399.72 MHz, CH_3OD): δ = 2.72 (brs, 20H*, CH_2), 4.50 (s, 8H; NCH_2CO), 4.80 (s, 8H; CH_2), 7.80 (s, 4H, C*H*), 7.86 (s, 8H, C*H*) ppm, *peak overlaps with residual methanol peak; ^{13}C NMR (100.49 MHz, CH_3OD): δ = 43.5 (*C*H_2), 52.3 (*C*H_2), 59.5 (*C*H_2), 122.2 (*C*H), 125.2 (q, ^1J = 271 Hz, *C*F_3), 129.5 (*C*H), 133.3 (q, ^2J = 33 Hz, *C*CF_3), 144.3, 173.8 ppm; ^{19}F NMR (376 MHz, CH_3OD): δ = –62.5 (s, CF_3) ppm. HRMS (*m*/*z*): $[M + H]^+$ calcd for $C_{52}H_{48}O_4N_8F_{24}$, 1305.3494; found, 1305.3444.

Europium(III) 2,2′,2″,2‴-(1,4,7,10-tetraazacyclododecane-1,4,7,10-tetrayl) tetrakis-(N-(4- (trifluoromethyl)benzyl)acetamide) trichloride (3Eu^{III}). To a flask containing 2,2′,2″,2‴-(1,4,7,10-tetraazacyclododecane-1,4,7,10-tetrayl) tetrakis(N-(3,5-bis(trifluoromethyl)benzyl)acetamide) (0.5000 g, 0.3833 mmol) and $EuCl_3·6H_2O$ (0.1275 g, 0.3484 mmol), CH_3OH (4 mL) and CH_3CN (125 mL) were added. The resulting mixture was heated at 80 °C. After 24 h, the mixture was filtered while hot through a fine glass frit, and the solvent was evaporated under reduced pressure. The crude product was crystallized from acetonitrile to yield a white solid (230 mg, 45%). ^1H NMR (399.72 MHz, D_2O): δ = –12.27 (brs), –9.86 (brs), –8.79 (brs), –4.61 (brs), –3.46 (brs), 2.03 (brs), 3.11 (brs), 3.76 (brs), 7.01 (brs), 7.17 (brs), 21.58 (brs) ppm. ^{19}F NMR (376 MHz, D_2O): δ = –62.54 (s, CF_3) ppm. HRMS (*m*/*z*): $[M – 3Cl]^{3+}$ calcd for $C_{52}H_{48}EuF_{24}N_8O_4Cl_3$, 485.7543; found, 485.7537 with expected isotope pattern. Elemental analysis (calculated, found for $C_{52}H_{48}F_{24}N_8O_4EuCl_3·6H_2O$): C (37.37, 37.02), H (3.62, 2.96), N (6.70, 6.66); TGA (*SI Appendix*, Fig. S3) shows a mass loss of 6.4%, corresponding to six molecules of H_2O, which is consistent with the elemental analysis data.

Europium(II) 2,2′,2″,2‴-(1,4,7,10-tetraazacyclododecane-1,4,7,10-tetrayl) tetrakis-(N-4-(trifluoromethyl)benzyl)acetamide) dichloride (3Eu^{II}). Under an atmosphere of N_2, a solution of **3Eu**^{III} (131.15 mg, 0.09 mmol) was prepared in water (10 mL, degassed), and the pH of the resulting solution was adjusted to 6.5 using HCl (1 M, degassed, aqueous). To the resulting solution, Zn dust (150 mg, 2.3 mmol) was added, and the mixture was stirred vigorously for 30 min. The mixture was filtered through a 0.2-μm filter, and the filtrate was swirled with DOWEX-Na^+ (0.1 g) for 1 min and filtered with a 0.2-μm filter. The DOWEX step was repeated a total of three times to yield a pale-yellow solution of **3Eu**^{II} (quantitative). Solutions of **3Eu**^{II} were characterized with luminescence spectroscopy to confirm loss of Eu^{III} (*SI Appendix*, Fig. S2), and the concentration of **3Eu**^{II} was determined with EDXF spectroscopy.

Crystallographic Data. A solution of either **1Eu**$^{III}Cl_3$ or **3Eu**$^{III}Cl_3$ (20 mg) in acetonitrile (15 drops) was filtered through a 0.2-μm hydrophilic filter into a 5-mm NMR tube. After evaporation, colorless crystals of **1Eu**$^{III}Cl_3$ and yellow color crystals of **3Eu**$^{III}Cl_3$ formed. A solution of **1Eu**$^{II}Cl_2$ in methanol was filtered through a 0.2-μm hydrophilic filter into a 5-mm NMR tube. Yellow-colored crystals formed in a desiccator placed in a wet glove box under N_2 atmosphere.

1Eu$^{III}Cl_3$ and **1Eu**$^{II}Cl_2$ were mounted on a MicroMount (MiTeGen) with paratone oil (Parabar 10312, Hampton Research) on a Bruker X8 APEX-II diffractometer with Mo radiation and a graphite monochromator. The X-ray diffraction intensities were measured using a Bruker APEX-II CCD detector. **3Eu**$^{III}Cl_3$ was mounted on a MicroMount (MiTeGen) with paratone oil (Parabar 10312, Hampton Research) on a Bruker D8 Venture diffractometer with kappa geometry, an Incoatec IμS microfocus source X-ray tube (Mo K_α radiation), and a multilayer mirror for monochromatization. All data were acquired with an Oxford 800 Cryostream low-temperature apparatus. The intensities were integrated using SAINT, and a multiscan absorption correction was applied with SADABS using Apex 3. The structures were solved by Intrinsic Phasing using ShelXT (46) and refined with ShelXL (47) using Olex2 (48).

All nonhydrogen atoms were refined anisotropically. The hydrogen atoms were positioned with idealized geometry and refined isotropically using a riding model. **1Eu**$^{III}Cl_3$ was modeled with whole molecule disorder over 4 sites (0.247:0.240:0.250:262). **1Eu**$^{II}Cl_2$ was a superstructure and was a pseudo-merohedral twin, as determined by Platon's TwinRotMat with a twin law of (1 0 0, 0 −1 0, 1 0 −1), and was refined with a batch scale factor of 0.742(5). **3Eu**$^{III}Cl_3$ had a disordered acetonitrile that could not be modeled, so a solvent mask in Olex2 was used and half of an acetonitrile molecule per formula unit was removed. The $–CF_3$ groups were disordered over 2 or 3 sites and the crystal was treated as an inversion twin with a 0.039(12) batch scale factor.

Convection-enhanced delivery of 1Eu^{II}. For convection-enhanced delivery, we used a Harvard Apparatus PHD 2000 infusion system to infuse 120 μL at a rate of 1.5 μL/min. Infusion catheters were placed such that the tip of the catheter was in the center of the tumor.

Hypoxia MRI. For assessment of hypoxia after convection-enhanced delivery, we generated T_1 maps of tumors. We also measured the ^{19}F signal using CSI. We conducted these measurements 1-h post convection-enhanced delivery. *T_1 measurements*. Standard rapid acquisition with relaxation pulse sequences were used, and T_1 maps were acquired and processed using Paravision 360 software. $1/T_1$ maps and $1/T_1$ difference maps were calculated using Image J.*^{19}F imaging (CSI).* ^{19}F-magnetic resonance spectroscopic imaging was performed using a fast spin echo imaging sequence with the following imaging parameters: field of view = 32 mm × 32 mm; image size = 16 × 16 voxels, slice thickness = 15 mm; repetition time = 250 ms; echo time = 0.647 ms; number of averages = 8; 1,024 free induction decay data points, spectral width = 25 kHz. 19F overlays and signal intensities were generated and measured using Osirix.

Validation of imaging with pimonidazole staining (hypoxyprobe). Pimonidazole staining was performed using the Hypoxyprobe kit (HP1-100Kit) per manufacturer's protocol. After MRI, tumors were extracted and sliced to align with MR images. To validate the hypoxia imaging, we performed pimonidazole staining

for in-situ detection of hypoxic regions within the tumors. Specifically, pimonidazole hydrochloride (60 mg/kg per manufacturer's recommendation) was injected via tail vein 60 to 90 min prior to killing the mouse. Subsequently, immunohistochemistry staining using Mab1 clone 4.3.11.3 was used to stain and confirm areas of hypoxia with MRI data (*SI Appendix*, Fig. S4).

Data, Materials, and Software Availability. All study data are included in the article and/or *SI Appendix*.

ACKNOWLEDGMENTS. We acknowledge the NIH (R01EB026453) for financial support. The Lumigen Instrument Center X-ray crystallography lab is partially supported by the NIH (3R01EB027103-02S1), and NMR lab is partially supported by the NIH (S10OD028488). A.G.S. was supported by the NIH (T32GM142519). We thank the Small Animal Imaging facility at Texas Children's Hospital as well as the Baylor College of Medicine Small Animal MRI ATC Core for access to imaging equipment and image-processing resources.

Author affiliations: [a]Department of Chemistry, Wayne State University, Detroit, MI 48202; [b]Department of Integrative Physiology, Baylor College of Medicine, Houston, TX 77030; [c]Lumigen Instrument Center, Wayne State University, Detroit, MI 48202; [d]Department of Pediatrics, Texas Children's Cancer Center, Baylor College of Medicine, Houston, TX 77030; and [e]Aflac Cancer and Blood Disorders Center, Children's Healthcare of Atlanta, Emory University School of Medicine, Atlanta, GA 30322

1. J.-N. Liu, W. Bu, J. Shi, Chemical design and synthesis of functionalized probes for imaging and treating tumor hypoxia. *Chem. Rev.* **117**, 6160–6224 (2017).
2. K. L. Eales, K. E. R. Hollinshead, D. A. Tennant, Hypoxia and metabolic adaptation of cancer cells. *Oncogenesis* **5**, e190 (2016).
3. S. A. Nabavizadeh *et al.*, Arterial spin labeling and dynamic susceptibility contrast-enhanced MR imaging for evaluation of arteriovenous shunting and tumor hypoxia in glioblastoma. *Sci. Rep.* **9**, 1–8 (2019).
4. C. T. Taylor, C. C. Scholz, The effect of HIF on metabolism and immunity. *Nat. Rev. Nephrol.* **18**, 573–587 (2022).
5. F. Paredes, H. C. Williams, A. S. Martin, Metabolic adaptation in hypoxia and cancer. *Cancer Lett.* **502**, 133–142 (2021).
6. Z. Zeng *et al.*, Hypoxic exosomal HIF-1α-stabilizing circZNF91 promotes chemoresistance of normoxic pancreatic cancer cells via enhancing glycolysis. *Oncogene* **40**, 5505–5517 (2021).
7. R. G. Bristow, R. P. Hill, Hypoxia, DNA repair and genetic instability. *Nat. Rev. Cancer* **8**, 180–192 (2008).
8. V. Bhandari *et al.*, Molecular landmarks of tumor hypoxia across cancer types. *Nat. Genet.* **51**, 308–318 (2019).
9. S. A. A. S. Subasinghe, R. G. Pautler, M. A. H. Samee, J. T. Yustein, M. J. Allen, Dual-mode tumor imaging using probes that are responsive to hypoxia-induced pathological conditions. *Biosensors* **12**, 478 (2022).
10. L. Qiu *et al.*, Tumor microenvironment responsive "head-to-foot" self-assembly nanoplatform for positron emission tomography imaging in living subjects. *ACS Nano* **15**, 18250–18259 (2021).
11. J. Liu *et al.*, Tumor microenvironment modulation platform based on composite biodegradable bismuth–manganese radiosensitizer for inhibiting radioresistant hypoxic tumors. *Small* **17**, 2101015 (2021).
12. X. Yang *et al.*, An oxygen-enriched thermosensitive hydrogel for the relief of a hypoxic tumor microenvironment and enhancement of radiotherapy. *Biomater. Sci.* **9**, 7471–7482 (2021).
13. Y. Zhang *et al.*, Rational construction of a reversible arylazo-based NIR probe for cycling hypoxia imaging in vivo. *Nat. Commun.* **12**, 1–10 (2021).
14. J. Wahsner, E. M. Gale, A. Rodríguez-Rodríguez, P. Caravan, Chemistry of MRI contrast agents: Current challenges and new frontiers. *Chem. Rev.* **119**, 957–1057 (2019).
15. A. Barandov *et al.*, Sensing intracellular calcium ions using a manganese-based MRI contrast agent. *Nat. Commun.* **10**, 1–9 (2019).
16. V. C. Pierre, S. M. Harris, S. L. Pailloux, Comparing strategies in the design of responsive contrast agents for magnetic resonance imaging: A case study with copper and zinc. *Acc. Chem. Res.* **51**, 342–351 (2018).
17. D. Xie, M. Yu, R. T. Kadakia, E. L. Que, ^{19}F Magnetic resonance activity-based sensing using paramagnetic metals. *Acc. Chem. Res.* **53**, 2–10 (2019).
18. R. Botár *et al.*, Stable and inert Mn(II)-based and pH-responsive contrast agents. *J. Am. Chem. Soc.* **142**, 1662–1666 (2020).
19. S. Guo *et al.*, Reductive microenvironment responsive gadolinium-based polymers as potential safe MRI contrast agents. *Biomater. Sci.* **7**, 1919–1932 (2019).
20. H. Wang *et al.*, Ultrasensitive magnetic resonance imaging of systemic reactive oxygen species in vivo for early diagnosis of sepsis using activatable nanoprobes. *Chem. Sci.* **10**, 3770–3778 (2019).
21. M. M. Rashid *et al.*, Systemic delivery of divalent europium from ligand screening with implications to direct imaging of hypoxia. *J. Am. Chem. Soc.* **144**, 23053–23060 (2022).
22. L. A. Basal *et al.*, Fluorinated Eu^{II}-based multimodal contrast agent for temperature- and redox-responsive magnetic resonance imaging. *Chem. Sci.* **8**, 8345–8350 (2017).
23. L. A. Ekanger *et al.*, Spectroscopic characterization of the +3 and +2 oxidation states of europium in a macrocyclic tetraglycinate complex. *Inorg. Chem.* **55**, 9981–9988 (2016).
24. L. A. Ekanger, L. A. Polin, Y. Shen, E. M. Haacke, M. J. Allen, Evaluation of Eu(II)-based positive contrast enhancement after intravenous, intraperitoneal, and subcutaneous injections. *Contrast Media Mol. Imaging* **11**, 299–303 (2016).
25. L. A. Ekanger *et al.*, A Eu(II)-containing cryptate as a redox sensor in magnetic resonance imaging of living tissue. *Angew. Chem. Int. Ed.* **54**, 14398–14401 (2015).
26. C. U. Lenora, Structural features of Europium(II)-containing cryptates that influence relaxivity. *Chem. Eur. J.* **23**, 15404–15414 (2017).
27. L. A. Ekanger, M. J. Allen, Overcoming the concentration-dependence of responsive probes for magnetic resonance imaging. *Metallomics* **7**, 405–421 (2015).
28. T. P. L. Roberts, Physiologic measurements by contrast-enhanced MR imaging: Expectations and limitations. *J. Magn. Res. Imaging* **7**, 82–90 (1997).
29. N. Raghunand, C. Howison, A. D. Sherry, S. Zhang, R. J. Gillies, Renal and systemic pH imaging by contrast-enhanced MRI. *Magn. Reason. Med.* **49**, 249–257 (2003).
30. E. Gianolio *et al.*, Dual MRI-SPECT agent for pH-mapping. *Chem. Commun.* **47**, 1539–1541 (2011).
31. L. Frullano, C. Catana, T. Benner, A. D. Sherry, P. Caravan, Bimodal MR–PET agent for quantitative pH imaging. *Angew. Chem. Int. Ed.* **49**, 2382–2384 (2010).
32. E. Gianolio, R. Napolitano, F. Fedeli, F. Arena, S. Aime, Poly-β-cyclodextrin based platform for pH mapping via a ratiometric ^{19}F/^{1}H MRI method. *Chem. Commun.* **40**, 6044–6046 (2009).
33. L. A. Ekanger, M. M. Ali, M. J. Allen, Oxidation-responsive $Eu^{2+/3+}$-liposomal contrast agent for dual-mode magnetic resonance imaging. *Chem. Commun.* **50**, 14835–14838 (2014).
34. A. E. Thorarinsdottir, K. Du, J. H. Collins, T. D. Harris, Ratiometric pH imaging with a Co^{II}_2 MRI probe via CEST effects of opposing pH dependences. *J. Am. Chem. Soc.* **139**, 15836–15847 (2017).
35. D. Janasik *et al.*, Ratiometric pH-responsive ^{19}F magnetic resonance imaging contrast agents based on hydrazone switches. *Anal. Chem.* **94**, 3427–3431 (2022).
36. N. Genicio, M. Bañobre-López, O. Gröhn, J. Gallo, Ratiometric magnetic resonance imaging: Contrast agent design towards better specificity and quantification. *Coord. Chem. Rev.* **447**, 214150 (2021).
37. Đ Toljić, G. Angelovski, A low-molecular-weight ditopic MRI probe for ratiometric sensing of zwitterionic amino acid neurotransmitters. *Chem. Commun.* **55**, 11924–11927 (2019).
38. L. Connah, G. Angelovski, Synergy of key properties promotes dendrimer conjugates as prospective ratiometric bioresponsive magnetic resonance imaging probes. *Biomacromolecules* **19**, 4668–4676 (2018).
39. O. A. Blackburn *et al.*, Substituent effects on fluoride binding by lanthanide complexes of DOTA-tetraamides. *Dalton Trans.* **45**, 3070–3077 (2016).
40. K. Srivastava, E. A. Weitz, K. L. Peterson, M. Marjańska, V. C. Pierre, Fe-and Ln-DOTAm-F12 are effective paramagnetic fluorine contrast agents for MRI in water and blood. *Inorg. Chem.* **56**, 1546–1557 (2017).
41. A. L. Thompson *et al.*, On the role of the counter-ion in defining water structure and dynamics: Order, structure and dynamics in hydrophilic and hydrophobic gadolinium salt complexes. *Dalton Trans.* **47**, 5605–5616 (2006).
42. R. S. Dickins *et al.*, Structural rigidity and luminescence of chiral lanthanide tetraamide complexes based on 1,4,7,10-tetraazacyclododecane. *Angew. Chem. Int. Ed.* **36**, 521–523 (1997).
43. C. Yang *et al.*, Bone microenvironment and osteosarcoma metastasis. *Int. J. Mol. Sci.* **21**, 6985 (2020).
44. L. Yu, J. Zhang, Y. Li, Effects of microenvironment in osteosarcoma on chemoresistance and the promise of immunotherapy as an osteosarcoma therapeutic modality. *Front. Immunol.* **13**, 871076 (2022).
45. W. Zhang *et al.*, Hypoxia-immune-related microenvironment prognostic signature for osteosarcoma. *Front. Cell Dev. Biol.* **10**, 974851 (2022).
46. G. M. Sheldrick, SHELXT- Integrated space-group and crystal structure determination. *Acta Cryst.* **71**, 3–8 (2015).
47. G. M. Sheldrick, Crystal structure refinement with SHELXL. *Acta Cryst.* **71**, 3–8 (2015).
48. O. V. Dolomanov, L. J. Bourhis, R. J. Gildea, J. A. K. Howard, H. Puschmann, OLEX2: A complete structure solution refinement and analysis program. *J. Appl. Cryst.* **42**, 339–341 (2009).